

Quantum Flow Matching

Zidong Cui,^{1,2} Pan Zhang,^{3,4} and Ying Tang^{1,2,5,*}

¹*Institute of Fundamental and Frontier Sciences,*

University of Electronic Science and Technology of China, Chengdu 611731, China

²*Key Laboratory of Quantum Physics and Photonic Quantum Information, Ministry of Education,
University of Electronic Science and Technology of China, Chengdu 611731, China*

³*Institute of Theoretical Physics, Chinese Academy of Sciences, Beijing 100190, China*

⁴*School of Fundamental Physics and Mathematical Sciences,*

Hangzhou Institute for Advanced Study, UCAS, Hangzhou 310024, China

⁵*School of Physics, University of Electronic Science and Technology of China, Chengdu 611731, China*

Flow matching has rapidly become a dominant paradigm in classical generative modeling, offering an efficient way to interpolate between two complex distributions. We extend this idea to the quantum realm and introduce Quantum Flow Matching (QFM)—a fully quantum-circuit realization that offers efficient interpolation between two density matrices. QFM offers systematic preparation of density matrices and generation of samples for accurately estimating observables, and can be realized on a quantum computer without the need for costly circuit redesigns. We validate its versatility on a set of applications: (i) generating target states with prescribed magnetization and entanglement entropy, (ii) estimating nonequilibrium free-energy differences to test the quantum Jarzynski equality, and (iii) expediting the study on superdiffusion breakdown. These results position QFM as a unifying and promising framework for generative modeling across quantum systems.

Introduction – The density matrix ρ is key to describing finite-temperature quantum systems [1, 2]. Preparing a target $\rho = \sum_i p_i |\psi_i\rangle\langle\psi_i|$ as an ensemble of pure states and estimating observables from it [3] depend on two critical factors: determining the probability p_i and preparing the pure state $|\psi_i\rangle$. Modern generative models [4] offer a route to capture both factors, including classical neural networks for ground-state search [5, 6] and tracking ρ 's dynamics [7]; tensor networks for thermal state simulation [8]; and quantum-classical hybrid models such as β -VQE [9] that integrate quantum circuits to estimate observables. Yet, these approaches are largely classical, leaving fully quantum protocols less explored. Typical quantum methods approximate p_i via statistical sampling, such as the minimally entangled typical thermal state (METTS) algorithm [10, 11] that employs a Markov chain. However, preparing states in the ensemble remains nontrivial and costly in these methods, since each pure state demands a tailored quantum circuit, leading to repeated circuit adjustments and significant overhead, especially in tasks such as estimating free energy changes [12] and studying phase transitions [13]. These challenges call for more efficient fully-quantum protocols to prepare and track ρ .

A quantum generative model that prepares ρ with a single circuit would be an efficient framework aligned well with quantum platforms, potentially bypassing the bottleneck of circuit adjustments. The recent quantum denoising diffusion probabilistic model (QuDDPM) [14] generates state ensembles by evolving from Haar-random states [15, 16], analogous to Gaussian noise classically. However, QuDDPM's inverse sampling prepares only the target ensemble, without capturing the time evolution of the target system, limiting its use in scenarios requiring flexible initialization or precise state control [17–19]. In

contrast, classical flow matching [20, 21], which learns flows to map between distributions, provides an effective alternative. Extending this idea to the quantum realm may overcome aforementioned limitations and broaden applications in quantum dynamics.

In this paper, we introduce QFM, a quantum counterpart of classical flow matching. Including QuDDPM as a special case initialized from the Haar-random ensemble, QFM enables the time evolution from input ensembles of an initial density matrix toward target ensembles. It learns the density matrix propagator step by step, either analytically from the Hamiltonian or through data-driven training. We employ its capability of evolving state ensembles to tackle diverse tasks, such as preparing thermal-state density matrices to estimate nonequilibrium free energy for testing the quantum Jarzynski equality [12], with reduced circuit-adjustment cost. We also apply it to capture superdiffusive scaling [19] by a fixed training-free circuit. For the comparison with QuDDPM, we demonstrate QFM on tasks including a topological state evolution, simulating entanglement growth, and the magnetic phase transition in the transverse-field Ising model (TFIM) [22]. We further provide theoretical bounds of QFM's generalization error in End Matter, supporting its wider applicability.

Quantum flow matching – QFM is designed to evolve a density matrix and learn each step of the evolution. We introduce it by an illustrative example of the time evolution of ring-shaped state ensembles (Fig. 1a). Starting from a density matrix ρ_0 approximated by an ensemble of M sampled pure states $S_0 = \{|\psi_0^1\rangle, \dots, |\psi_0^M\rangle\}$, QFM evolves each $|\psi_0^m\rangle$ independently over \mathcal{T} steps with a fixed circuit, yielding a final ensemble $S_{\mathcal{T}} = \{|\psi_{\mathcal{T}}^1\rangle, \dots, |\psi_{\mathcal{T}}^M\rangle\}$ that approximates the target density matrix $\rho_{\mathcal{T}}$. At selected steps (Fig. 1b), QFM dynamically employs ancilla

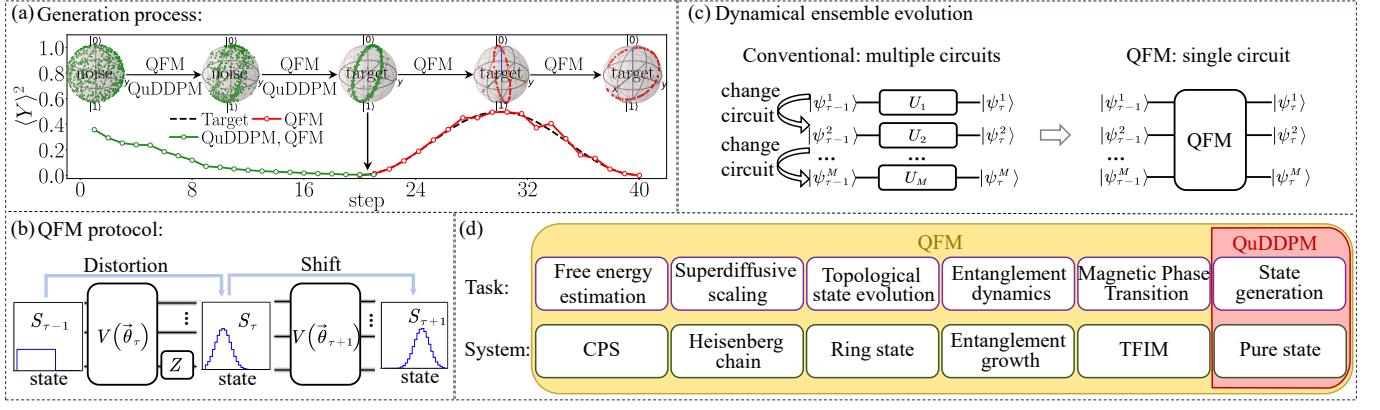


FIG. 1. Schematic of quantum flow matching. (a) QFM learns the evolution between two density matrices, as the quantum counterpart of classical flow matching [20]. Different from QuDDPM [14], QFM does not require starting from the Haar-random ensemble, allowing wider applications. (b) QFM alternatively applies partly measured circuits and unitary circuits to ensure convergency and stability. (c) QFM employs a single quantum circuit to emulate the time evolution of the density matrix, alleviating extensive circuit adjustments. The symbol i denotes time steps, and M is the index of states. (d) QFM can estimate free energy and probe superdiffusive scaling (main text), as well as evolve topological state ensembles, control entanglement entropy, and track magnetic phase transition (Supplemental Material [22]).

qubits whose measurement outcomes condition the circuit evolution on the initial state, thereby shaping the state distribution. This adaptive protocol evolves arbitrary density matrices, correspondingly the state ensembles, through a single circuit (Fig.1c), enabling diverse applications (Fig.1d).

Circuit structure – The circuit of QFM can be fixed analytically or trainable, depending on the target problem. For the ensemble of Hamiltonians differing only in local terms, we tend to construct circuits without training; for more general cases, we employ the training protocol. Specifically, we denote the circuit at step τ as $V(\vec{\theta}_\tau)$ with the parameter vector $\vec{\theta}_\tau$. The circuits with n_a ancilla qubits are written as $V(\vec{\theta}_\tau) = U_{n_a}(\vec{\theta}_\tau)$, while those acting only on n data qubits are $V(\vec{\theta}_\tau) = U_n(\vec{\theta}_\tau)$. For problems such as the superdiffusion breakdown, $V(\vec{\theta}_\tau)$ can be tailored to have an analytically fixed circuit structure. By measuring ancilla qubits, QFM generates an ensemble of distinct Hamiltonian evolutions with a single circuit.

For problems requiring a trainable circuit, such as estimating the free energy change, QFM employs an L -layer entanglement-varied hardware-efficient ansatz (EHA) [23] at each step, with $\vec{\theta}_\tau$ as trainable parameters. Each layer of EHA applies single-qubit gates $U^{(1)} = \prod_{j \in \{x,y,z\}} \exp\{-i\theta_j \sigma_j / 2\}$ to each qubit, followed by gates $U^{(2)} = \prod_{j \in \{x,y,z\}} \exp\{-i\theta_j \sigma_j \otimes \sigma_j / 2\}$ sequentially on all nearest-neighbor pairs, with $\theta_j \in \vec{\theta}_\tau$ and Pauli operator σ_j . When $V(\vec{\theta}_\tau) = U_n(\vec{\theta}_\tau)$, QFM applies the EHA directly on data qubits. When $V(\vec{\theta}_\tau) = U_{n_a}(\vec{\theta}_\tau)$, measuring ancilla qubits is equivalent to inserting a single-qubit gate $U_{(r_{n_a})}$ between $U^{(1)}$ and $U^{(2)}$ on the data qubit neighboring with ancilla qubits in each layer. The gate $U_{(r_{n_a})} = \exp\{-i\theta(-1)^{r_{n_a}} \sigma_z / 2\}$, whose

structure depends on the measurement result $r_{n_a} \in \{0, 1\}$ of the n_a -th ancilla qubit. If $U^{(2)}$ is allowed to couple each ancilla qubit with data qubits rather than nearest neighbors, $U_{(r_{n_a})}$ becomes dependent on all ancilla measurement outcomes, increasing its expressive ability and circuit depth. Training details are in the End Matter.

Generation – Starting from an initial state $|\psi_0^m\rangle \in S_0$, QFM sequentially applies $V(\vec{\theta}_1^{\text{op}}) \cdots V(\vec{\theta}_{\tau-1}^{\text{op}})$ to generate $|\tilde{\psi}_{\tau-1}^m\rangle \in \tilde{S}_{\tau-1}$, where the tilde indicates results generated by QFM and the superscript of $\vec{\theta}_\tau^{\text{op}}$ denotes “optimized”. QFM uses a hybrid approach to construct $V(\vec{\theta}_\tau^{\text{op}})$, which switches between two types of circuits. The first is a partially measured circuit, where n_a ancilla qubits initialized by rotation operator $R_y(\theta) = \exp(-i\theta \sigma_y / 2)$ to get $R_y^{\otimes n_a}(\tau\pi/T)|0\rangle^{\otimes n_a}$ are projectively measured along the z -axis after evolving $|\tilde{\psi}_\tau^m\rangle = U_{n_a}(\vec{\theta}_\tau^{\text{op}})|0\rangle^{\otimes n_a}|\tilde{\psi}_{\tau-1}^m\rangle \in \tilde{S}_\tau$. The second is a unitary circuit, where we directly apply the circuit on n data qubits, e.g., the EHA circuit in trainable cases.

Applications – We demonstrate the method by applying it to representative tasks. The main text focuses on free energy estimation (with a variational circuit) and superdiffusive scaling (with a fixed circuit). The remaining examples, which serve as benchmarks to compare QFM with QuDDPM, are listed in End Matter and detailed in Supplemental Material [22]. The ring-state evolution illustrates QFM’s capability to map between two quantum state ensembles, beyond QuDDPM requiring starting from a Haar-random ensemble. QFM also allows the generation of states with specific entanglement entropy and the control of entanglement growth from separable to maximally entangled states. QFM further learns the evolution from an ordered ferromagnetic phase to a disordered phase, capturing the phase transition.

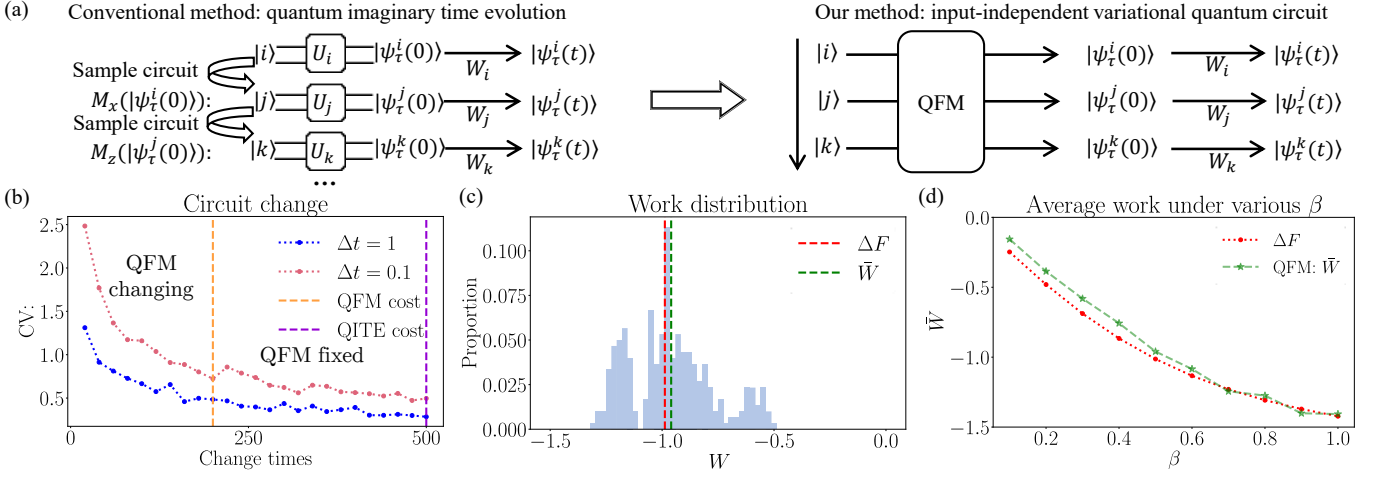


FIG. 2. QFM efficiently estimates nonequilibrium free energy changes. (a) Free energy is estimated via sampling pseudo-thermal states in METTS. Left: The conventional method [12] of quantum imaginary time evolution (QITE) [24, 25] requires repeatedly adjusting quantum circuits to generate each pseudo-thermal state. Right: QFM generates an ensemble of pseudo-thermal states using a fixed circuit post-training. (b) The coefficient of variation (CV), under the time evolution with duration $\Delta t = 1$ (blue) and $\Delta t = 0.1$ (red) at $\beta = 1.5$, shows that QFM converges with around 200 circuit updates (orange), whereas QITE requires 500 times (purple) [12]. The gap widens with a shorter duration of time evolution. (c) For $\beta = 0.5$, the expectation (green) of work distribution (bar) matches closely with the theoretical free energy change ΔF (red). (d) Free energy changes agree with the averaged work across inverse temperatures β . The simulation is conducted for a 4-qubit TFIM.

QFM facilitates free energy estimation – The celebrated Jarzynski equality [26] enables to calculate the free energy change between two equilibrium states, from the work in the nonequilibrium process. In quantum simulations, the quantum Jarzynski equality [27–30] is typically tested by computing the average work \bar{W} from evolving METTS [10–12] under a time-dependent Hamiltonian $H(t)$. METTS are prepared via QITE starting from classical product states (CPS), e.g., $|i\rangle$, sampled through alternating M_x and M_z measurements. This requires repeatedly adjusting the QITE circuit for each sample to achieve thermalization (Fig. 2a, left), with the number of circuit changes scaling with the number of samples, incurring substantial experimental overhead.

QFM can generate the METTS ensemble with a single circuit (Fig. 2a right). Starting from an initial state $|i\rangle$, QFM sequentially applies $V(\vec{\theta}_1^{\text{op}}) \cdots V(\vec{\theta}_\tau^{\text{op}})$ to generate the target METTS $|\psi_\tau^m\rangle$ at inverse temperature β_τ , and prepares the next input state $|j\rangle$ by measurement. The parameter $\vec{\theta}_\tau^{\text{op}}$ is obtained by minimizing the loss function $D(\vec{\theta}_\tau) = (1/M) \sum_{m=1}^M \langle \psi_\tau^m | V(\vec{\theta}_\tau) | \tilde{\psi}_{\tau-1}^m \rangle$ with the training data $S_\tau = \{|\psi_\tau^m\rangle \mid |\psi_\tau^m\rangle = A^{-1} e^{-\beta_\tau H(0)} |i\rangle, |i\rangle \in \text{CPS}\}$ prepared by QITE and $A = \sqrt{\langle \psi_\tau^m | e^{-\beta_\tau H(0)} | \psi_\tau^m \rangle}$, followed by real-time evolution to get $|\psi_\tau^m(t)\rangle$. Details of the training procedure are in the End Matter.

For a TFIM $H(t) = \sum_i \sigma_z^i \sigma_z^{i+1} + g(t) \sum_i \sigma_x^i$ with transverse field strength $g(t) = 1 + t/20$ ($t = 0 \rightarrow 10$), QFM generates METTS ensembles \tilde{S}_τ at inverse temperatures $\beta_\tau = \tau/\mathcal{T}$ for $\mathcal{T} = 10$ and $L = 20$. In Fig. 2b ($\beta = 1$), as \bar{W} converges (stabilized coefficient of variation), QFM

including circuit adjustments during training still reduces total circuit adjustments by 60% compared with conventional methods [10, 11], with greater savings for faster time evolution. Putting the training process on a classical computer can further alleviate the cost of circuit adjustments. QFM accurately generates the average work matching with the analytical free energy change both at $\beta = 0.5$ (Fig. 2c) and across temperatures (Fig. 2d).

Superdiffusive scaling estimation – Quantum simulation has recently enabled the study of superdiffusive behavior [19]. Using QFM, we examine how superdiffusion breakdown depends on the strength and type of interactions in the 2D Heisenberg model, obtained by extending a Floquet-type 1D system. In the limit of vanishing 2D interaction strength J_\perp (black box in Fig. 3a), the model reduces to an infinite-temperature 1D Heisenberg chain with interaction strength J . The first-order Trotterization with \mathcal{T} steps is

$$e^{-iH_{2D}(t)} = \left(e^{-iH_a t/\mathcal{T}} e^{-iH_c t/\mathcal{T}} e^{-iH_b t/\mathcal{T}} \right)^\mathcal{T}, \quad (1)$$

where $H_k = \sum_{\langle i,j \rangle \in k} h_{i,j}$ for $k \in \{a, b, c\}$ denotes the Hamiltonian with bonds of type k , and the two-qubit interaction $h_{i,j}(\vec{J}) = (J/4) \sum_{j=x,y,z} \lambda_j \sigma_j^i \sigma_j^j$ has parameters $\vec{\lambda} = (\lambda_x, \lambda_y, \lambda_z)$. The 1D interactions are fixed as $\vec{J} = (1, 1, 1) \times J$, and the 2D-interaction is $\vec{J}_\perp = \vec{\lambda} \times J_\perp$. For the 10-qubit system in Fig. 3a, the 1D interactions include $\langle 2, 3 \rangle$, $\langle 5, 6 \rangle$, $\langle 10, 11 \rangle$ in type a ; $\langle 3, 4 \rangle$, $\langle 6, 7 \rangle$, $\langle 8, 9 \rangle$ in type c ; and $\langle 4, 5 \rangle$, $\langle 7, 8 \rangle$, $\langle 9, 10 \rangle$ in type b . The 2D interaction is in type a with location $\langle 4, 9 \rangle$.

The conventional simulations on superdiffusion scaling

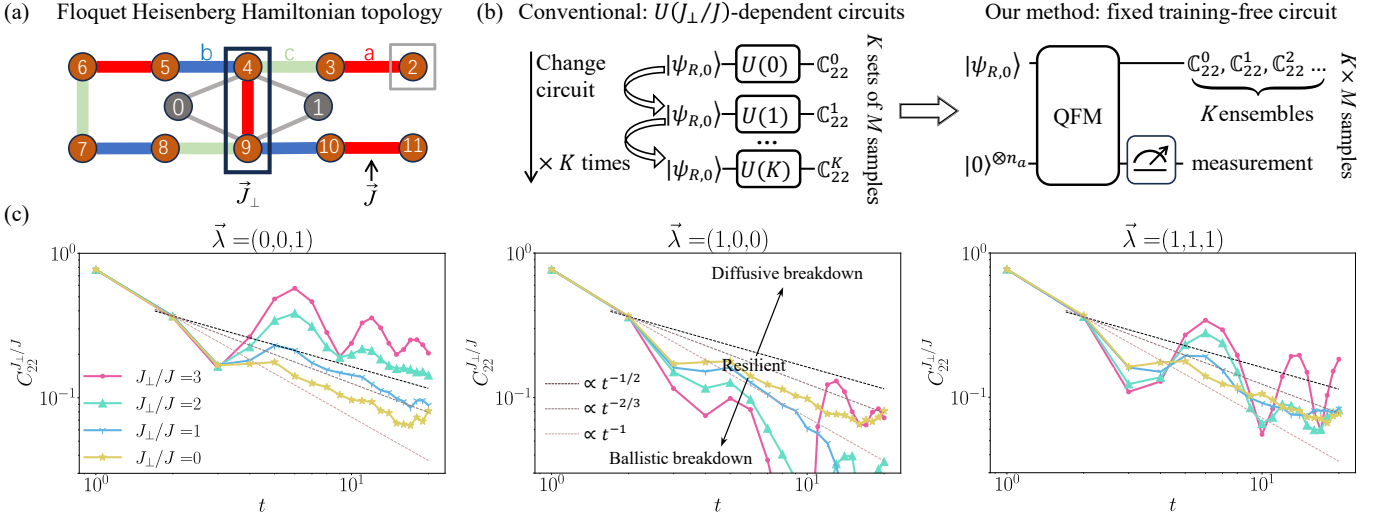


FIG. 3. QFM facilitates the estimation of superdiffusive scaling. (a) The conventional method [19] requires adjusting the quantum circuits for a Heisenberg model under various 2D-interaction strengths (black box). (b) QFM evolves the state ensemble with a fixed circuit and adjusts the 2D-interaction strength by measurements on ancilla qubits (gray node in (a)). (c) The diffusive behaviors by QFM for 2D-interaction strengths $J_{\perp}/J \in \{0, 1, 2, 3\}$ in three interaction types, matching the conventional method [19]. Increasing J_{\perp}/J accentuates both diffusive ($\vec{\lambda} = (0, 0, 1)$) and ballistic ($\vec{\lambda} = (1, 0, 0)$) breakdowns. In the resilient case ($\vec{\lambda} = (1, 1, 1)$), stronger 2D interactions enlarge the variance of the superdiffusive scaling.

require K circuits, each of which evaluates the correlation function $C_{22}^{J_{\perp}/J}$ (End Matter) at distinct J_{\perp}/J values with M random states $|\psi_{R,0}\rangle$. If we consider $J_{\perp}/J \in \{0, 1, 2, 3\}$ and $\mathcal{T} = 20$, the quantum circuit is:

$$U(J_{\perp}/J) = (U_{1D}(a)U_{2D}(a)U_{1D}(c)U_{1D}(b))^{\mathcal{T}}, \quad (2)$$

$$U_{1D}(a) = \prod_{\text{a type}} \exp\{-ih_{i,j}(\vec{J})\}, \quad (3)$$

$$U_{2D}(a) = \exp\{-ih_{4,9}(\vec{J})\}. \quad (4)$$

It requires repeated adjustments on the circuit that increase the experimental overhead (Fig. 3b left).

QFM realizes the same task with a single fixed circuit (Fig. 3b right), without a substantial circuit depth increase. It introduces two ancilla qubits (grey nodes in Fig. 3a) and adjusts the 2D-interaction strength through measurements, enabling uniform J_{\perp}/J sampling without sampling cost. The QFM circuit over steps 1 to τ is

$$\begin{aligned} U_{n_a}(\tau) = & \left[U_{1D}(a) \times \exp\{-i[\sigma_z^0 + 0.5\sigma_z^1] \otimes h_{4,9}(\vec{J}_{\perp})\} \right. \\ & \times \exp\{-i \times 1.5h_{4,9}(\vec{J}_{\perp})\} \\ & \left. U_{1D}(c)U_{1D}(b) \right]^{\tau} H_{\text{gate}}^0 H_{\text{gate}}^1, \end{aligned} \quad (5)$$

where H_{gate}^0 and H_{gate}^1 are Hadamard gates that act on qubit 0 and 1 to balance the probability of each measurement result. After measurements, the circuit becomes:

$$U_{n_a}(\tau) = (U_{1D}(a)U_{2D}(a)U_{1D}(c)U_{1D}(b))^{\tau}, \quad (6)$$

$$\begin{aligned} U_{2D}(a) = & \exp\{-i[(-1)^{r_0} + 0.5(-1)^{r_1}] \otimes h_{4,9}(\vec{J}_{\perp})\} \\ & \times \exp\{-i \times 1.5h_{4,9}(\vec{J}_{\perp})\}, \end{aligned} \quad (7)$$

where each r_i with $i \in \{0, 1\}$ is sampled independently and uniformly from $\{0, 1\}$, producing circuits corresponding to $J_{\perp}/J = 0, 1, 2, 3$.

We show how interaction strengths affect superdiffusion in Fig. 3c. For $\vec{\lambda} = (0, 0, 1)$, the system exhibits diffusive breakdown at $J_{\perp}/J \geq 2$. For $\vec{\lambda} = (1, 0, 0)$, ballistic transport breaks down at $J_{\perp}/J \geq 1$. The system remains resilient for $\vec{\lambda} = (1, 1, 1)$. Thus, QFM achieves consistent results by a single circuit, eliminating the multiple circuits required by conventional methods [19].

Conclusion – We have presented a quantum generative model QFM for transforming between two density matrices and tracking the time evolution of state distributions. Compared with the classical neural-network approaches [4, 7, 31, 32] and quantum-classical models [11, 12, 33], QFM employs a single quantum circuit and provides more efficient estimations of observables. We have demonstrated QFM’s capabilities in learning topological state evolution, magnetic phase-transition simulation, and entanglement-entropy growth. Especially, QFM can bypass costly circuit adjustments to estimate free energy changes and superdiffusive scaling, offering a promising approach to track nonequilibrium quantum dynamics with less experimental overhead. While current hardware may constrain fault-tolerant implementations on quantum processors, the advances in device performance [34–36] and quantum error correction [37–40] are expected to mitigate these constraints. Future directions include experimental implementations of QFM and its application to facilitate the simulation of a broader class of quantum dynamics.

Acknowledgments – We acknowledge Lei Wang and Xiaopeng Li for helpful discussions. This work is supported by Projects 12322501, 12325501 of the National Natural Science Foundation of China. The computational work is supported by the Center for HPC, University of Electronic Science and Technology of China.

* Corresponding authors: jamestang23@gmail.com

- [1] A. Polkovnikov, K. Sengupta, A. Silva, and M. Vengalattore, Colloquium: Nonequilibrium dynamics of closed interacting quantum systems, *Rev. Mod. Phys.* **83**, 863 (2011).
- [2] L. D'Alessio, Y. Kafri, A. Polkovnikov, and M. Rigol, From quantum chaos and eigenstate thermalization to statistical mechanics and thermodynamics, *Adv. Phys.* **65**, 239 (2016).
- [3] M. C. Banuls, R. Blatt, J. Catani, A. Celi, J. I. Cirac, M. Dalmonte, L. Fallani, K. Jansen, M. Lewenstein, S. Montangero, *et al.*, Simulating lattice gauge theories within quantum technologies, *Eur. Phys. J. D* **74**, 1 (2020).
- [4] G. Carleo, I. Cirac, K. Cranmer, L. Daudet, M. Schuld, N. Tishby, L. Vogt-Maranto, and L. Zdeborová, Machine learning and the physical sciences, *Rev. Mod. Phys.* **91**, 045002 (2019).
- [5] K. Choo, G. Carleo, N. Regnault, and T. Neupert, Symmetries and many-body excitations with neural-network quantum states, *Phys. Rev. Lett.* **121**, 167204 (2018).
- [6] G. Torlai, G. Mazzola, J. Carrasquilla, M. Troyer, R. Melko, and G. Carleo, Neural-network quantum state tomography, *Nat. Phys.* **14**, 447 (2018).
- [7] M. Schmitt and M. Heyl, Simulating dynamics of correlated matter with neural quantum states, *arXiv:2506.03124* (2025).
- [8] F. Verstraete, J. J. García-Ripoll, and J. I. Cirac, Matrix product density operators: Simulation of finite-temperature and dissipative systems, *Phys. Rev. Lett.* **93**, 207204 (2004).
- [9] J.-G. Liu, L. Mao, P. Zhang, and L. Wang, Solving quantum statistical mechanics with variational autoregressive networks and quantum circuits, *Mach. Learn.: Sci. Technol.* **2**, 025011 (2021).
- [10] E. Stoudenmire and S. R. White, Minimally entangled typical thermal state algorithms, *New J. Phys.* **12**, 055026 (2010).
- [11] S. R. White, Minimally entangled typical quantum states at finite temperature, *Phys. Rev. Lett.* **102**, 190601 (2009).
- [12] L. Bassman Oftelie, K. Klymko, D. Liu, N. M. Tubman, and W. A. de Jong, Computing free energies with fluctuation relations on quantum computers, *Phys. Rev. Lett.* **129**, 130603 (2022).
- [13] J. C. Getelina, N. Gomes, T. Iadecola, P. P. Orth, and Y.-X. Yao, Adaptive variational quantum minimally entangled typical thermal states for finite temperature simulations, *SciPost Phys.* **15**, 102 (2023).
- [14] B. Zhang, P. Xu, X. Chen, and Q. Zhuang, Generative quantum machine learning via denoising diffusion probabilistic models, *Phys. Rev. Lett.* **132**, 100602 (2024).
- [15] F. G. Brandao, A. W. Harrow, and M. Horodecki, Local random quantum circuits are approximate polynomial-designs, *Commun. Math. Phys.* **346**, 397 (2016).
- [16] P. Ćwikliński, M. Horodecki, M. Mozrymas, L. Pankowski, and M. Studziński, Local random quantum circuits are approximate polynomial-designs: numerical results, *Phys. A: Math. Theor.* **46**, 305301 (2013).
- [17] S. Lloyd, Universal quantum simulators, *Science* **273**, 1073 (1996).
- [18] A. Schuckert, O. Katz, L. Feng, E. Crane, A. De, M. Hafezi, A. V. Gorshkov, and C. Monroe, Observation of a finite-energy phase transition in a one-dimensional quantum simulator, *Nat. Phys.* **21**, 374 (2025).
- [19] K. Kumaran, M. Sajjan, B. Pokharel, J. Gibbs, J. Cohn, B. Jones, S. Mostame, S. Kais, and A. Banerjee, Quantum simulation of superdiffusion breakdown in heisenberg chains via 2d interactions, *arXiv:2503.14371* (2025).
- [20] Y. Lipman, R. T. Chen, H. Ben-Hamu, M. Nickel, and M. Le, Flow matching for generative modeling, *arXiv:2210.02747* (2022).
- [21] D. Rezende and S. Mohamed, Variational inference with normalizing flows, in *Proceedings of the 32nd International Conference on Machine Learning*, Proceedings of Machine Learning Research, Vol. 37, edited by F. Bach and D. Blei (PMLR, Lille, France, 2015) pp. 1530–1538.
- [22] *See Supplemental Material at [URL will be inserted by publisher] for details on the quantum circuit, applications to generating the ring-state evolution, controlling the entanglement growth, and tracking the magnetic phase transition.*
- [23] X. Wang, B. Qi, Y. Wang, and D. Dong, Entanglement-variational hardware-efficient ansatz for eigensolvers, *Phys. Rev. Appl.* **21**, 034059 (2024).
- [24] M. Motta, C. Sun, A. T. Tan, M. J. O'Rourke, E. Ye, A. J. Minnich, F. G. Brandao, and G. K.-L. Chan, Determining eigenstates and thermal states on a quantum computer using quantum imaginary time evolution, *Nat. Phys.* **16**, 205 (2020).
- [25] S. McArdle, T. Jones, S. Endo, Y. Li, S. C. Benjamin, and X. Yuan, Variational ansatz-based quantum simulation of imaginary time evolution, *npj Quantum Inf.* **5**, 75 (2019).
- [26] C. Jarzynski, Nonequilibrium equality for free energy differences, *Phys. Rev. Lett.* **78**, 2690 (1997).
- [27] J. Kurchan, A quantum fluctuation theorem, *arXiv cond-mat/0007360* (2000).
- [28] H. Tasaki, Jarzynski relations for quantum systems and some applications, *arXiv cond-mat/0009244* (2000).
- [29] S. Mukamel, Quantum extension of the jarzynski relation: Analogy with stochastic dephasing, *Phys. Rev. Lett.* **90**, 170604 (2003).
- [30] P. Talkner, E. Lutz, and P. Hänggi, Fluctuation theorems: Work is not an observable, *Phys. Rev. E* **75**, 050102 (2007).
- [31] D. Luo, Z. Chen, J. Carrasquilla, and B. K. Clark, Autoregressive neural network for simulating open quantum systems via a probabilistic formulation, *Phys. Rev. Lett.* **128**, 090501 (2022).
- [32] Y. Tang, J. Liu, J. Zhang, and P. Zhang, Learning nonequilibrium statistical mechanics and dynamical phase transitions, *Nat. Commun.* **15**, 1117 (2024).
- [33] E. Zapusek, K. Kirova, W. Hahn, M. Marthaler, and F. Reiter, Variational quantum thermalizers based on

- weakly-symmetric nonunitary multi-qubit operations, arXiv:2502.09698 (2025).
- [34] A. D. King, A. Nocera, M. M. Rams, J. Dziarmaga, R. Wiersema, W. Bernoudy, J. Raymond, N. Kaushal, N. Heinsdorf, R. Harris, *et al.*, Beyond-classical computation in quantum simulation, *Science* **388**, 199 (2025).
 - [35] X. Wu, C. Zhu, J. Wang, and X. Wang, Boss: Blocking algorithm for optimizing shuttling scheduling in ion trap, arXiv:2412.03443 (2024).
 - [36] D. Gao and et al., Establishing a new benchmark in quantum computational advantage with 105-qubit zuchongzhi 3.0 processor, *Phys. Rev. Lett.* **134**, 090601 (2025).
 - [37] R. Acharya, D. A. Abanin, L. Aghababaie-Beni, I. Aleiner, T. I. Andersen, M. Ansmann, F. Arute, K. Arya, A. Asfaw, N. Astrakhantsev, *et al.*, Quantum error correction below the surface code threshold, *Nature* **638**, 920 (2025).
 - [38] S. Bravyi, A. W. Cross, J. M. Gambetta, D. Maslov, P. Rall, and T. J. Yoder, High-threshold and low-overhead fault-tolerant quantum memory, *Nature* **627**, 778 (2024).
 - [39] H. Cao, F. Pan, D. Feng, Y. Wang, and P. Zhang, Generative decoding for quantum error-correcting codes, arXiv:2503.21374 (2025).
 - [40] P. Zhang, Correcting a noisy quantum computer using a quantum computer, arXiv:2506.08331 (2025).
 - [41] E. Grant, L. Wossnig, M. Ostaszewski, and M. Benedetti, An initialization strategy for addressing barren plateaus in parametrized quantum circuits, *Quantum* **3**, 214 (2019).
 - [42] J. Benton, G. Deligiannidis, and A. Doucet, Error bounds for flow matching methods, arXiv:2305.16860 (2023).
 - [43] M. C. Caro, H.-Y. Huang, N. Ezzell, J. Gibbs, A. T. Sornborger, L. Cincio, P. J. Coles, and Z. Holmes, Out-of-distribution generalization for learning quantum dynamics, *Nat. Commun.* **14**, 3751 (2023).
 - [44] J. Richter and A. Pal, Simulating hydrodynamics on noisy intermediate-scale quantum devices with random circuits, *Phys. Rev. Lett.* **126**, 230501 (2021).
 - [45] A. Nahum, J. Ruhman, S. Vijay, and J. Haah, Quantum entanglement growth under random unitary dynamics, *Phys. Rev. X* **7**, 031016 (2017).
 - [46] J. Carrasquilla and R. G. Melko, Machine learning phases of matter, *Nat. Phys.* **13**, 431 (2017).
 - [47] W. Roga, D. Spehner, and F. Illuminati, Geometric measures of quantum correlations: characterization, quantification, and comparison by distances and operations, *J. Phys. A: Math. Theor.* **49**, 235301 (2016).
 - [48] J. Ho, A. Jain, and P. Abbeel, Denoising diffusion probabilistic models, in *Advances in Neural Information Processing Systems*, Vol. 33, edited by H. Larochelle, M. Ranzato, R. Hadsell, M. Balcan, and H. Lin (Curran Associates, Inc., 2020) pp. 6840–6851.
 - [49] Y. Song, J. Sohl-Dickstein, D. P. Kingma, A. Kumar, S. Ermon, and B. Poole, Score-based generative modeling through stochastic differential equations, in *Proceedings of the 9th International Conference on Learning Representations (ICLR)* (2021).
 - [50] A. Kandala, A. Mezzacapo, K. Temme, M. Takita, M. Brink, J. M. Chow, and J. M. Gambetta, Hardware-efficient variational quantum eigensolver for small molecules and quantum magnets, *nature* **549**, 242 (2017).
 - [51] R. Wiersema, C. Zhou, Y. de Sereville, J. F. Carrasquilla, Y. B. Kim, and H. Yuen, Exploring entanglement and optimization within the hamiltonian variational ansatz, *PRX Quantum* **1**, 020319 (2020).
 - [52] C. Lyu, X. Xu, M.-H. Yung, and A. Bayat, Symmetry enhanced variational quantum spin eigensolver, *Quantum* **7**, 899 (2023).
 - [53] J. Romero, R. Babbush, J. R. McClean, C. Hempel, P. J. Love, and A. Aspuru-Guzik, Strategies for quantum computing molecular energies using the unitary coupled cluster ansatz, *Quantum Sci. Technol.* **4**, 014008 (2018).
 - [54] J. M. Arrazola, O. Di Matteo, N. Quesada, S. Jahangiri, A. Delgado, and N. Killoran, Universal quantum circuits for quantum chemistry, *Quantum* **6**, 742 (2022).
 - [55] A. J. McRoberts and R. Moessner, Parametrically long lifetime of superdiffusion in nonintegrable spin chains, *Phys. Rev. Lett.* **133**, 256301 (2024).
 - [56] M. Schuld and N. Killoran, Quantum machine learning in feature hilbert spaces, *Phys. Rev. Lett.* **122**, 040504 (2019).
 - [57] S. Lloyd, S. Garnerone, and P. Zanardi, Quantum algorithms for topological and geometric analysis of data, *Nat. commun.* **7**, 10138 (2016).
 - [58] H.-Y. Huang, M. Broughton, M. Mohseni, R. Babbush, S. Boixo, H. Neven, and J. R. McClean, Power of data in quantum machine learning, *Nat. commun.* **12**, 2631 (2021).
 - [59] J. Zhang, G. Pagano, P. W. Hess, A. Kyprianidis, P. Becker, H. Kaplan, A. V. Gorshkov, Z.-X. Gong, and C. Monroe, Observation of a many-body dynamical phase transition with a 53-qubit quantum simulator, *Nature* **551**, 601 (2017).
 - [60] F. Arute, K. Arya, R. Babbush, D. Bacon, J. C. Bardin, R. Barends, R. Biswas, S. Boixo, F. G. Brandao, D. A. Buell, *et al.*, Quantum supremacy using a programmable superconducting processor, *Nature* **574**, 505 (2019).
 - [61] H. J. Kimble, The quantum internet, *Nature* **453**, 1023 (2008).
 - [62] S. Wehner, D. Elkouss, and R. Hanson, Quantum internet: A vision for the road ahead, *Science* **362**, eaam9288 (2018).
 - [63] M. Z. Hasan and C. L. Kane, Colloquium: Topological insulators, *Rev. Mod. Phys.* **82**, 3045 (2010).
 - [64] Z.-Y. Wang, X.-C. Cheng, B.-Z. Wang, J.-Y. Zhang, Y.-H. Lu, C.-R. Yi, S. Niu, Y. Deng, X.-J. Liu, S. Chen, *et al.*, Realization of an ideal weyl semimetal band in a quantum gas with 3d spin-orbit coupling, *Science* **372**, 271 (2021).

END MATTER

TABLE I: Glossary of mathematical terms.

Notion	Description
ρ_0	the density matrix at step 0
n	the number of data qubits
n_a	the number of ancilla qubits
σ_z^i	Pauli operator Z on qubit i
S_τ	the state ensemble at step τ
M	number of states in one ensemble
$ \psi_\tau^m\rangle$	a sample state in S_τ
\mathcal{T}	the number of steps
θ	one parameter in $\vec{\theta}_\tau$
$\vec{\theta}_\tau$	the parameter vector at step τ
$\vec{\theta}_\tau^{\text{op}}$	the optimized parameter vector
$V(\vec{\theta}_\tau)$	the circuit in step τ of QFM
L	the layer number of EHA in each step
$U_{n_a}(\vec{\theta}_\tau)$	the circuit with ancilla qubits
$U_n(\vec{\theta}_\tau)$	the circuit only acts on data qubits
$U^{(1)}$	single-qubit gate in EHA
$U^{(2)}$	two-qubit gate in EHA
$U_{(r)}$	the measurement-induced gate
r_{n_a}	the measurement result of the n_a -th qubit
R_y	the rotation operator about the y axis
$ \tilde{\psi}_\tau^m\rangle$	the generated state in step τ
\tilde{S}_τ	the generated ensemble in step τ
M_z	measurement along the Z direction
$D(\vec{\theta}_\tau)$	loss function
$H(t)$	time-dependent Hamiltonian
$g(t)$	transverse field strength
β_τ	inverse temperature
J	1D-interaction strength
J_\perp	2D-interaction strength
K	number of different interaction ratio J_\perp/J
$C_{22}^{J_\perp/J}$	correlation function with prob qubit 2
a, b, c	the bonds of the Hamiltonian

Training detail – We provide details on the training of QFM, with all the mathematical symbols summarized in Table I. After completing the training up to step $\tau - 1$, we proceed to train the $V(\vec{\theta}_\tau)$ at step τ . We sequentially apply operators from $V(\vec{\theta}_1^{\text{op}})$ to $V(\vec{\theta}_{\tau-1}^{\text{op}})$, generating the state ensemble $S_{\tau-1} = \{|\tilde{\psi}_{\tau-1}^1\rangle, \dots, |\tilde{\psi}_{\tau-1}^M\rangle\}$. We then apply $U_n(\vec{\theta}_\tau)$ to states sampled from $S_{\tau-1}$ and minimize the loss function $D(\vec{\theta}_\tau)$ to get the $\vec{\theta}_\tau^{\text{op}}$. If $D(\vec{\theta}_\tau^{\text{op}})$ is lower than the threshold \mathbb{T}_τ , $U_n(\vec{\theta}_\tau^{\text{op}})$ will be the τ -th step of QFM; otherwise, we switch $U_n(\vec{\theta}_\tau^{\text{op}})$ to $U_{n_a}(\vec{\theta}_\tau)$ and repeat the same training process with input state $\tilde{S}_{\tau-1}^{n_a} = \{|0\rangle^{\otimes n_a} |\tilde{\psi}_{\tau-1}^1\rangle, \dots, |0\rangle^{\otimes n_a} |\tilde{\psi}_{\tau-1}^M\rangle\}$. To avoid barren plateaus, we initialize parameters in each layer with a neighborhood of radius $\mathcal{O}(1/L)$ [41]. We determine the τ -th step parameter $\vec{\theta}_\tau$ by minimizing the loss function:

$$E_m = O_\tau(|\psi_\tau^m\rangle, V(\vec{\theta}_\tau) |0\rangle^{\otimes n_a} |\tilde{\psi}_{\tau-1}^m\rangle), \quad (8)$$

$$\vec{\theta}_\tau^{\text{op}} = \min_{\vec{\theta}_\tau} D(\vec{\theta}_\tau) = \min_{\vec{\theta}} f_\tau(E_1, E_2, \dots, E_M), \quad (9)$$

where O and f are the operator and the function depending on the application. For examples requiring the fidelity estimation, O is the swap-test operator and f is the average function. For the example of entanglement growth, O estimates the entanglement entropy of $|\psi_\tau^m\rangle$ and f is the mean squared error (MSE).

Generalization error – We analyze the bound on the generalization error [42, 43] of QFM for training-based tasks. To learn a unitary $U_\tau \in \mathcal{U}$ at step τ , we have a training set $S_\tau = \{(|\psi_\tau^m\rangle, U_\tau |\psi_\tau^m\rangle)\}_{m=1}^M$. The training cost is:

$$D(\vec{\theta}_\tau^{\text{op}}) = \frac{1}{4M} \sum_{m=1}^M \|U_\tau |\psi_\tau^m\rangle \langle \psi_\tau^m| U_\tau^\dagger - V(\vec{\theta}_\tau^{\text{op}}) |\tilde{\psi}_\tau^m\rangle \langle \tilde{\psi}_\tau^m| V(\vec{\theta}_\tau^{\text{op}})^\dagger\|_1^2. \quad (10)$$

The distance between $V(\vec{\theta}_\tau^{\text{op}})$ and target unitary U_τ gives the expected risk:

$$R_{P_\tau}(\vec{\theta}_\tau^{\text{op}}) = \frac{1}{4} \mathbb{E}_{|\Psi_\tau\rangle \sim P} \left[\|U_\tau |\Psi_\tau\rangle \langle \Psi_\tau| U_\tau^\dagger - V(\vec{\theta}_\tau^{\text{op}}) |\Psi_\tau\rangle \langle \Psi_\tau| V(\vec{\theta}_\tau^{\text{op}})^\dagger\|_1^2 \right], \quad (11)$$

where P_τ is the test set at step τ . For a \mathcal{N} -gate unitary layer $U_n(\vec{\theta}_\tau^{\text{op}})$ in QFM, the expected risk $R_P^n(\vec{\theta}_\tau^{\text{op}})$ obeys:

$$R_P^n(\vec{\theta}) \leq 2D_\tau(\vec{\theta}_\tau^{\text{op}}) + \mathcal{O}\left(\sqrt{\frac{\mathcal{N} \log(\mathcal{N})}{M}}\right). \quad (12)$$

For partially measured layer $U_{n_a}(\vec{\theta}_\tau^{\text{op}})$, the expected risk $R_P^{n_a}(\vec{\theta}_\tau^{\text{op}})$ satisfies:

$$\mathbb{E}_\tau = \frac{1}{M} \sum_{m=1}^M \left| \langle \psi_\tau^m | U_{n_a}^\dagger(\vec{\theta}_\tau^{\text{op}}, m_{n_a}) U_\tau |\psi_\tau^m\rangle \right|^2, \quad (13)$$

$$D_\tau^{n_a}(\vec{\theta}_\tau^{\text{op}}) = 1 - \mathbb{E}_\tau, \quad (14)$$

$$R_P^{n_a}(\vec{\theta}_\tau^{\text{op}}) \leq 2D_\tau^{n_a}(\vec{\theta}_\tau^{\text{op}}) + \mathcal{O}\left(\sqrt{\frac{\mathcal{N}_{\text{eff}} \log(\mathcal{N}_{\text{eff}})}{M}}\right), \quad (15)$$

where \mathcal{N}_{eff} is the number of gates in the U_{n_a} without ancilla qubits.

Correlation function for superdiffusive scaling – The correlation function can be expressed as a single-point observable [44]:

$$C_{pp}(t) = \frac{1}{2M} \sum \langle \psi_{R,p} | \sigma_z^p | \psi_{R,p} \rangle, \quad (16)$$

where $|\psi_{R,p}\rangle = |0\rangle_p |\psi_R\rangle$, the $|\psi_R\rangle$ is a Haar-random state, and p is the location of the probe qubit. In the example of Fig. 3, the correlation function is evaluated using 100 states per interaction strength, with $p = 2$ and $M = 100$ for each interaction strength.

TABLE II. Hyperparameters and results in the three examples. Here, n is the number of data qubits, n_a is the number of ancilla qubits, M is the number of training states, and L is the number of layers in each step of QFM.

Task	n	n_a	L	O	f	\mathcal{T}	M	Performace
Ring state ensemble evolution	1	0	5	Swap test	Arithmetic Mean	20	100	0.037
Entanglement growth	2	1	40	Entanglement entropy estimation	MSE	10	100	0.012
Magnetic Phase Transition	[2, 11]	1	20	Energy estimation	Arithmetic Mean	15	100	0.035

More applications – To demonstrate the method, we apply QFM to three additional examples of pure-state generation. Its ability to map between multiple quantum state ensembles leads to improved performance over QuDDOM in each example. We briefly introduce the examples and summarize QFM’s performance in Table II. More details of each example are given in Supplemental Material [22].

In the ring-state evolution example, QFM learns an ensemble rotating along the Z -axis on the Bloch sphere. For entanglement growth, QFM is used to increase the entanglement entropy of a two-qubit system over 10 steps [45]. In the magnetic phase transition example, QFM generates ground-state ensembles and measures the magnetization $M = (\sum_i Z_i)/n$ across varying qubit numbers ($n \in [2, 11]$) and field strengths ($g = 0.0 \rightarrow 1.5$).

In each example, we evaluate the performance of QFM by the mean Kullback–Leibler (KL)-divergence [46] between the generated and target distributions of an observable during the time evolution. The observable depends on the task: measurement results in the Y -direction for ring-state evolution, entanglement entropy for entanglement growth, and magnetization for the magnetic phase transition. We consider the KL-divergence below 0.05 to indicate reliable distributional matching. Besides the KL-divergence, alternative metrics such as the Hellinger distance [47] or trace distance can also be employed, which provide qualitatively consistent results.

SUPPLEMENTAL MATERIAL FOR “QUANTUM FLOW MATCHING”

Flow matching generative model and Diffusion generative model

Flow-matching and diffusion generative models are two major paradigms in generative modeling. Flow-matching [20] learns a continuous vector field $v(x, t)$ that transports samples x_t from any source distribution $p_0(x)$ to any target distribution $p_1(x)$ by solving the ordinary differential equation (ODE)

$$\frac{dx_t}{dt} = v(x_t, t), \quad x_0 \sim p_0(x),$$

with the objective of minimizing the mismatch between the pushed-forward prior and the target distribution along the trajectory. In contrast, diffusion generative models [48, 49] define a forward stochastic process that gradually adds noise to the data and learns a reverse denoising process $\hat{p}(x_{t-1}|x_t)$ from Gaussian noise to the target, typically optimized via the variational objective:

$$\mathcal{L}_{\text{diffusion}} = \mathbb{E}_{x_0, \epsilon, t} [\|\epsilon - \epsilon_\theta(x_t, t)\|^2],$$

where ϵ is the noise in this step.

The key difference lies in the generation mechanism: flow-matching is deterministic and can map between *arbitrary* distributions, enabling direct interpolation, exact likelihood evaluation, and transformation between diverse data types. Diffusion, by contrast, generates samples stochastically, is restricted to starting from Gaussian noise, and typically requires many denoising steps to handle complex or multimodal distributions. For example, flow-matching can efficiently transform samples between different image classes, interpolate between embeddings in text or speech models, or morph between distinct multimodal datasets—tasks that diffusion models cannot perform directly.

Circuit structure

QFM employs two circuit designs: an entanglement-varied hardware-efficient ansatz (EHA) for training tasks, and a tailored structure for training-free cases such as simulating the 2D Heisenberg model in superdiffusive scaling. In this section, we will provide a detailed description of the structure of the EHA circuit, as well as the different circuit structures corresponding to the various measurement outcomes of the ancilla qubits. Meanwhile, we will take superdiffusive scaling as an example to illustrate how to design a training-free circuit, in which measurements on the ancilla qubits can modify the 2D interaction strength of the simulated system.

Circuit for variational quantum circuit

For training tasks, QFM employs the L -layer EHA circuit at each step. The EHA circuit employs variational entanglers composed of parameterized XX , YY , and ZZ gates. This design allows the circuit to rapidly adjust the amount of entanglement to match the target ground state, thereby overcoming limitations such as barren plateaus and poor trainability. Compared with widely used ansatzes, including HEA (hardware-efficient ansatz) [50], HVA (Hamiltonian variational ansatz) [51], HSA (hardware symmetry-preserving ansatz) [52], and chemically inspired ansatzes such as UCCSD (unitary coupled cluster with all single and double excitations) [53] and GRSD (Givens rotations with all single and double excitations) [54], EHA consistently achieves higher accuracy and greater robustness across both quantum many-body systems and molecular simulations. Importantly, EHA is problem-agnostic, making it broadly applicable without requiring specific prior knowledge of the Hamiltonian or tailored initial states.

Each layer of the EHA circuit includes arbitrary single-qubit rotations $U^{(1)} = \prod_{j \in \{x, y, z\}} \exp\{-i\theta_j \sigma_j / 2\}$ and nearest-neighbor two-qubit gates $U^{(2)} = \prod_{j \in \{x, y, z\}} \exp\{-i\theta_j \sigma_j \otimes \sigma_j / 2\}$. For intuitive understanding, we present in Fig. 4 the L -layer circuit structure of $U_n(\vec{\theta})$ for a three-qubit example, where each layer consists of arbitrary single-qubit gates and nearest-neighbor entangling gates along the X , Y , and Z directions. All θ parameters in the figure are trainable.

In Fig. 5, we illustrate how 2 ancilla qubits are coupled to 3 data qubits. After applying $U_n(\vec{\theta})$ on the data qubits, we first apply the single-qubit gates from the EHA circuit to each ancilla qubit. Then, on the ancilla qubits nearest to the data qubits, followed by XX , YY , and ZZ gates on the ancilla nearest the data qubits. The remaining ancilla qubits are similarly coupled sequentially to their nearest-neighbor ancilla qubits to construct the U_{n_a} . At the end of U_{n_a} , each ancilla qubit is measured in the Pauli- Z basis.

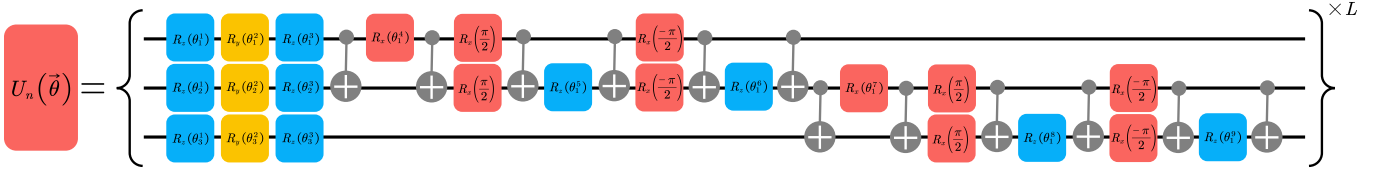


FIG. 4. Unitary circuit $U_n(\vec{\theta})$ in QFM. For steps without ancilla qubits in QFM, we apply the EHA circuit on data qubits. EHA includes layers of X and Y single-qubit rotations followed by nearest-neighbor gates XX , YY , and ZZ , which provide tunable entanglement in the x , y , and z directions.

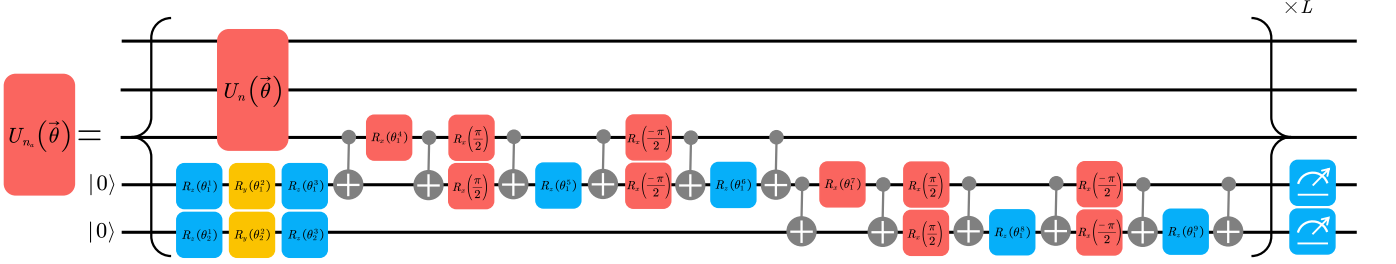


FIG. 5. The circuit structure of steps with n_a ancilla qubits in QFM. For U_{n_a} , we add n_a ancilla qubits, which are coupled to the data qubits through the same single- and two-qubit gates as in the EHA circuit, and measure the ancilla qubits with the Pauli- Z operator at the end of each step.

Circuit for 2D Heisenberg model

The one-dimensional (1D) isotropic Heisenberg chain, as an integrable model, exhibits anomalous superdiffusive spin transport characterized by Kardar-Parisi-Zhang (KPZ) universality. This phenomenon, initially predicted theoretically and observed experimentally in quasi-1D materials like KCuF_3 [55], is a cornerstone of nonequilibrium quantum many-body physics. However, real materials inherently host integrability-breaking interactions—such as interchain couplings in quasi-1D systems or engineered perturbations in quantum simulators—which disrupt superdiffusion and induce a crossover to conventional diffusive or ballistic transport. Understanding this breakdown is essential for connecting idealized theories to real-world quantum materials.

We employ QFM to probe how two-dimensional (2D) interactions, native to scalable hardware architectures like IBM's heavy-hex lattice, drive the suppression of superdiffusion. By tuning the strength and symmetry of these 2D couplings, we elucidate their role in destabilizing KPZ scaling. QFM employs a training-free circuit to simulate the 2D Heisenberg model with varying interaction strengths. By coupling ancilla qubits, the 2D interactions are adjusted based on their measurement outcomes. The circuit consists of a 1D interaction part U_{1D} and a 2D interaction part U_{2D} . We employ measurements on the ancilla qubits in QFM to modify the 2D interaction strength of the simulated

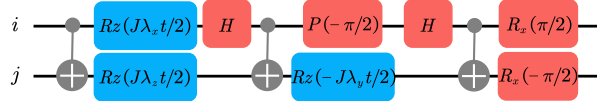


FIG. 6. Trotter circuit for time evolution of $h_{i,j}$ for time t

Heisenberg system on the data qubits. For clarity, we decompose the evolution operator into interaction operators along different bonds and dimensions. Since these interactions are local and mutually commuting, the first-order Trotter circuit for simulating the 2D Heisenberg model is:

$$U(J_{\perp}/J) = (U_{1D}(a)U_{2D}(a)U_{1D}(c)U_{1D}(b))^T. \quad (17)$$

In U_{1D} , there is a series of two-local terms $h_{i,j}$ acting on qubits i and j . Each two-local term also commutes with the others, so each can be represented by a corresponding evolution operator:

In U_{1D} , the Hamiltonian consists of a series of two-local terms $h_{i,j}$, each acting on qubits i and j . Since all these two-local terms mutually commute, the evolution under U_{1D} can be factorized such that each term is implemented

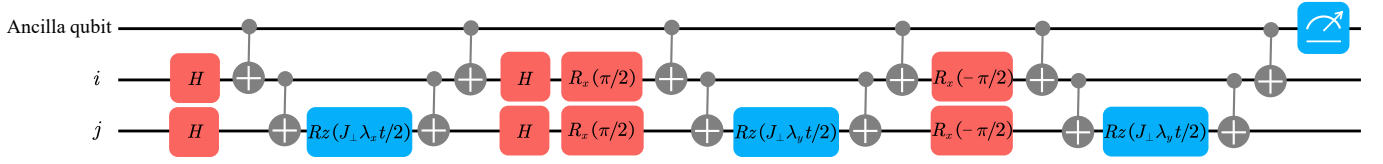


FIG. 7. Trotter circuit for the time evolution of 2D term in U_{n_a} for time t

independently. Specifically, each two-local term $h_{i,j}$ can be represented by a corresponding evolution operator $e^{-ih_{i,j}t}$, allowing the full unitary U_{1D} to be expressed as the product of these operators. This decomposition facilitates efficient circuit implementation and ensures exact simulation of the 1D interactions.

$$e^{-ih_{i,j}(\vec{J})t} = \exp \left\{ -iJ(\lambda_x \sigma_x^i \sigma_x^j + \lambda_y \sigma_y^i \sigma_y^j + \lambda_z \sigma_z^i \sigma_z^j)t/4 \right\}. \quad (18)$$

We implement the operator using first-order Trotter-Suzuki decomposition, as shown in Fig. 6. For the 2D interaction term U_{2D} , QFM adjusts the interaction strength based on measurements of ancilla qubits. In the main text example, the coupling strength between each ancilla qubit and the 2D system is parameterized by θ_i , with an additional drift term C applied to the 2D interaction:

$$U_{n_a}(\tau) = \left[U_{1D}(a) \times \exp \left\{ -i \frac{J_{\perp}}{4} [\theta_0(-1)^{r_0} + \theta_1(-1)^{r_1} + \theta_2(-1)^{r_2} + \theta_3(-1)^{r_3}] \otimes h_{4,9} \right\} \right. \quad (19)$$

$$\left. \times \exp \left\{ -i \frac{C}{4} J_{\perp} \times h_{4,9} \right\} U_{1D}(c) U_{1D}(b) \right]^{\tau}. \quad (20)$$

To implement different 2D interaction strengths $J_{\perp}/J = 0, 1, 2, 3$ conditioned on the outcomes of ancilla qubit measurements, we adjust the circuit parameters accordingly. Specifically, for the reference value $J = 1$, the single-qubit rotation angles θ_i and the coupling constant C are set to values that realize the desired interaction strength in the effective Hamiltonian. These parameter settings ensure that each measurement outcome on the ancilla qubits correctly tunes the two-dimensional coupling between data qubits.

$$\begin{cases} \theta_0 = 1, \\ \theta_1 = 0.5, \\ \theta_2 = \theta_3 = 0, \\ C = 1.5. \end{cases} \quad (21)$$

Furthermore, to avoid additional sampling overhead, it is necessary to generate a uniform distribution over J_{\perp}/J . This can be achieved by preparing each ancilla qubit in an equal superposition of its computational basis states, which is analogous to applying a Hadamard gate H_{gate} to each ancilla. In this way, all possible interaction strengths are sampled with equal probability without requiring repeated sampling or post-selection:

$$\begin{aligned} U_{n_a}(\tau) = & \left[U_{1D}(a) \times \exp \left\{ -i[\sigma_z^0 + 0.5\sigma_z^1] \otimes h_{4,9}(\vec{J}_{\perp}) \right\} \right. \\ & \times \exp \left\{ -i \times 1.5 h_{4,9}(\vec{J}_{\perp}) \right\} \\ & \left. U_{1D}(c) U_{1D}(b) \right]^{\tau} H_{\text{gate}}^0 H_{\text{gate}}^1, \end{aligned} \quad (22)$$

where the first-order Trotter-Suzuki decomposition of the 2D interaction terms in U_{n_a} is illustrated in Fig. 7, where the interactions along different bonds and directions are implemented sequentially. After measurements, the circuit will be:

$$\begin{aligned} U_{n_a}(\tau) = & (U_{1D}(a) U_{2D}(a) U_{1D}(c) U_{1D}(b))^{\tau} \\ U_{2D}(a) = & \exp \left\{ -i[(-1)^{m_0} + 0.5(-1)^{m_1}] \otimes h_{4,9}(\vec{J}_{\perp}) \right\} \\ & \times \exp \left\{ -i \times 1.5 h_{4,9}(\vec{J}_{\perp}) \right\}, \end{aligned} \quad (23)$$

where each r_i with $i \in \{0, 1\}$ is sampled independently with equal probability from $\{0, 1\}$. For the 2D interaction strength defined as $J_{\perp} = \theta_{a_0}(-1)^{r_0} + \theta_{a_1}(-1)^{r_1} + \theta_{a_2}(-1)^{r_2} + \theta_{a_3}(-1)^{r_3} + C$, the resulting distribution of J_{\perp} is

determined by the independent binary sampling of each r_i . This procedure ensures that all possible combinations of signs occur with equal probability, producing a discrete set of interaction strengths that can be used to implement a uniform or tailored ensemble of 2D couplings conditioned on the ancilla measurements:

$$\begin{aligned} p(r_0 = 0, r_1 = 0) &= 0.25 : J_{\perp} = 3, \\ p(r_0 = 0, r_1 = 1) &= 0.25 : J_{\perp} = 2, \\ p(r_0 = 1, r_1 = 0) &= 0.25 : J_{\perp} = 1, \\ p(r_0 = 1, r_1 = 1) &= 0.25 : J_{\perp} = 0. \end{aligned} \quad (24)$$

Performance of non-adaptive circuits in entanglement growth

At step τ , we adaptively select U_n and U_{n_a} to ensure convergence. U_n handles shifts in the state distribution from step $\tau - 1$, but cannot account for distortions, while U_{n_a} can approximate distorted distributions. However, using U_{n_a} on purely shifted distributions introduces fluctuations and hinders convergence. By appropriately choosing between U_n and U_{n_a} , we accurately map the state distribution from step $\tau - 1$ to τ .

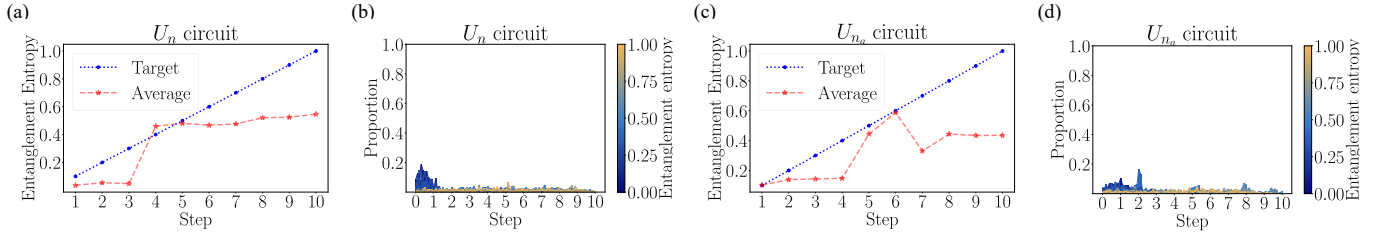


FIG. 8. The learning performance in entanglement growth for each step of QFM with only U_n and for each step of QFM with only U_{n_a} . Both circuits fail to learn the expected evolution process: the average entanglement entropy (red dashed line) does not match the target entanglement entropy (blue dashed line), and the entanglement entropy distribution of the generated states at each step does not concentrate around the target entanglement entropy.

We numerically compare circuits using only U_n with those using only U_{n_a} (QuDDPM) in generating entangled states. A circuit composed solely of U_n cannot distort the distribution of quantum states; therefore, the average entanglement entropy of the generated states fails to match the growth of the target entanglement entropy (Fig. 8a). This is reflected in the distributions at each step: in the early steps, the entanglement entropy of the generated states exhibits a peak concentrated near the target entanglement entropy, but in later steps the distribution gradually becomes uniform (Fig. 8b). We speculate that this is because, at the beginning, the growth of entanglement entropy is relatively small, so the target state distribution is not far from the initial state distribution, allowing some degree of fitting. However, for highly entangled states, the shape of the target distribution differs significantly from the initial distribution, leading to increasingly poor learning performance in subsequent steps. In contrast, a circuit composed solely of U_{n_a} tends to alter the shape of the state distribution at every step. This increases the training difficulty in steps where the distribution shape should ideally remain unchanged (Fig. 8c). Consequently, the generated states exhibit a large variance in entanglement entropy from the very beginning (Fig. 8d), highlighting the limitation of using a single type of circuit and highlights the need for carefully choosing the circuit structure at each step.

Work Estimation

The Jarzynski equality provides a remarkable connection between non-equilibrium processes and equilibrium free energy differences. It states that the exponential average of the work W performed on a system during a finite-time, non-equilibrium process satisfies:

$$\langle e^{-\beta W} \rangle = e^{-\beta \Delta F},$$

where β is the inverse temperature, ΔF is the free energy difference between the initial and final equilibrium states, and the average is taken over many realizations of the process. This equality implies that equilibrium free energy

differences can be obtained from measurements of work in arbitrarily far-from-equilibrium transformations, making it a powerful tool in both classical and quantum thermodynamics. It also underpins fluctuation theorems and has been widely applied in experimental and computational studies of small systems.

In quantum computation [27–29], the minimally entangled typical thermal states (METTS) algorithm provides an efficient way to sample from the thermal density matrix at inverse temperature β . The procedure begins by choosing a classical product state $|i\rangle$ in the computational basis, which is then evolved in imaginary time under the Hamiltonian H to obtain a normalized thermal-like state:

$$|\psi^0\rangle = \frac{e^{-\beta H/2}|i\rangle}{\|e^{-\beta H/2}|i\rangle\|}.$$

Repeated projective measurements in the computational basis collapse $|\psi^0\rangle$ to a new product state $|j\rangle$, which is then used to generate the next METTS. Iterating this process produces an ensemble of METTS $\{|\psi^m\rangle\}$ whose statistical properties approximate the thermal density matrix ρ_β .

To estimate free energy differences using the Jarzynski equality, each METTS $|\psi^m\rangle$ is evolved under a finite-time, non-equilibrium protocol corresponding to a Hamiltonian change, and the work W_m performed is recorded. The exponential average over the ensemble,

$$\langle e^{-\beta \bar{W}} \rangle \approx \frac{1}{M} \sum_{m=1}^M e^{-\beta W_m},$$

then provides an estimate of the free energy difference ΔF . This approach efficiently combines thermal-state sampling with quantum simulation of non-equilibrium dynamics, enabling accurate free energy estimation on quantum devices without requiring full thermal density matrix preparation. The thermal average of \bar{W} is estimated by evolving sufficiently METTS. The detailed estimation procedure by QFM is as follows:

Algorithm 1: Estimation of Thermal Average Work \bar{W} via QFM

Input: Inverse temperature β_τ , Hamiltonian $H(t)$

Output: Work samples $\{W_m\}$ and estimated average \bar{W}

for each sample index $m = 1$ to M **do**

- (1) QFM evolves a CPS state $|i\rangle$ into METTS $|\tilde{\psi}_\tau^m\rangle$;
- (2) Compute initial energy: $E_i = \langle \tilde{\psi}_\tau^m | H(0) | \tilde{\psi}_\tau^m \rangle$;
- (3) Apply real time-evolution to get: $|\tilde{\psi}_\tau^m(t)\rangle$;
- (4) Compute final energy: $E_f = \langle \tilde{\psi}_\tau^m(t) | H(t) | \tilde{\psi}_\tau^m(t) \rangle$;
- (5) Calculate work sample: $W_m = E_f - E_i$;
- (6) Measure $|\tilde{\psi}_\tau^m\rangle$ to obtain next CPS state;

end

Compute thermal average: $\bar{W} = (1/M) \sum_{m=1}^M W_m$.

For the example in the main text, we set $M = 300$ for each β_τ in a 4-qubit system.

More benchmarks for quantum flow matching

For comparison with QuDDPM, we applied QFM to three tasks: topological state evolution, entanglement growth, and the magnetic phase transition in the transverse-field Ising model (TFIM). QuDDPM, starting from a Haar-random ensemble, learns to generate a specific ring-state ensemble in the topological state evolution and a state ensemble with a given magnetization. In contrast, QFM can evolve between different target ensembles in both tasks and accomplish entanglement growth—a task that cannot be achieved using only U_{n_a} .

Ring state evolution: highlighting the difference from quantum denoising diffusion model

As the first application, we implement QFM to simulate the time evolution of quantum states with nontrivial topology, which appears when the classical data set is encoded in quantum states [56–58]. Specifically, we focus on the rotational dynamics of the Z -axis when encoding classical ring-shaped data distributions into quantum states,

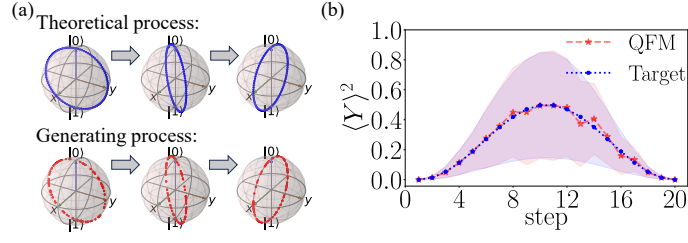


FIG. 9. Generation of ring state ensemble. (a) Blue dots are sample states used to train the model, and red dots are generated states. (b) The generated states (red) have matched deviation $\langle Y^2 \rangle$ with the theoretical values (blue).

preserving their topological connectivity through rotations of $\mathcal{T} = 20$ steps (Fig. 9a). The evolution starts from $S_0 = \{|\psi_0^m\rangle | |\psi_0^m\rangle = e^{-i\sigma_x G_m} |0\rangle, G_j \sim U(0, 2\pi)\}$ to $S_\tau = \{|\psi_\tau^m\rangle | |\psi_\tau^m\rangle = e^{-i\sigma_z G_\tau} |\psi_\tau^m\rangle, G_\tau = \pi\tau/\mathcal{T}\}$. The loss function of l -th step is chosen as $D(\vec{\theta}_l) = 1/M \sum_{m=1}^M \langle \psi_\tau^m | V(\vec{\theta}_\tau) | \tilde{\psi}_{\tau-1}^m \rangle$, leading to the generated ensembles in Fig. 9a. The performance of QFM is validated by the match of the deviation $\langle Y \rangle^2$ from the theoretical and generated results (Fig. 9b).

Entanglement growth: generating states with specific entanglement entropy

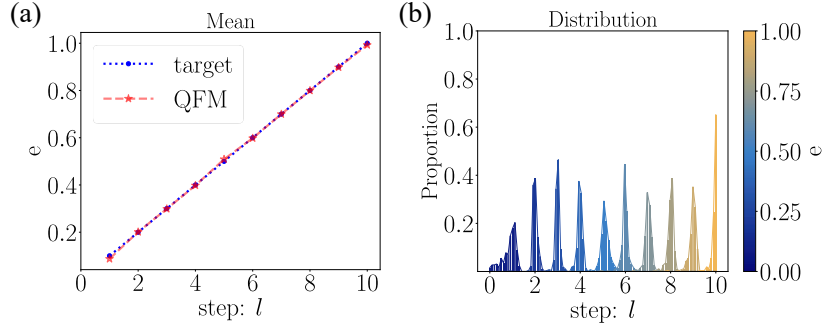


FIG. 10. Generation of entangled state ensembles. (a) Red dots are the average entanglement entropy of the generated state ensemble at various steps, and blue dots are the target entanglement entropy in each step. (b) The entanglement entropy distribution of the ensemble generated at each step is denoted by color.

Through dynamically tuned multi-body interactions in a layered quantum circuit architecture, our QFM realizes entanglement growth from separable states to maximally entangled states—a critical capability for scalable quantum network node preparation and fault-tolerant logic gate implementation [59–62]. We apply QFM to grow the entanglement entropy in a 2-qubit quantum system [45] in 10 steps. The loss function at the τ -th step is defined as $D(\vec{\theta}_\tau) = \frac{1}{M} \sum_{m=1}^M (e_\tau - \tilde{e}_\tau^m(\vec{\theta}_\tau))^2$, where $\tilde{e}_\tau^m(\vec{\theta}_\tau)$ corresponds to the entanglement entropy of the dynamically generated state $|\tilde{\psi}_\tau^m\rangle = V(\vec{\theta}_\tau^{op}) |\tilde{\psi}_{\tau-1}^m\rangle$ within the ensemble S_τ , while the target value e_τ scales linearly as τ/\mathcal{T} . As shown in Fig. 10a, the ensemble-averaged entanglement entropy (red) tracks its target linear growth (blue). In Fig. 10b, we show the distribution of states with certain entanglement entropy at each step.

Magnetic Phase Transition: capturing the phase transition

Magnetic phase transitions, driven by quantum-fluctuation-induced symmetry breaking, reveal universal scaling in collective spins and guide quantum material design with controlled quantum phases [63, 64]. For a transverse-field Ising model (TFIM) described by the Hamiltonian:

$$H(g) = - \sum_i \sigma_z^i \sigma_z^{i+1} - g \sum_i \sigma_x^i, \quad (25)$$

which undergoes a phase transition from the ordered ferromagnetic phase to the disordered phase with $g = 1$ (Fig. 11a).

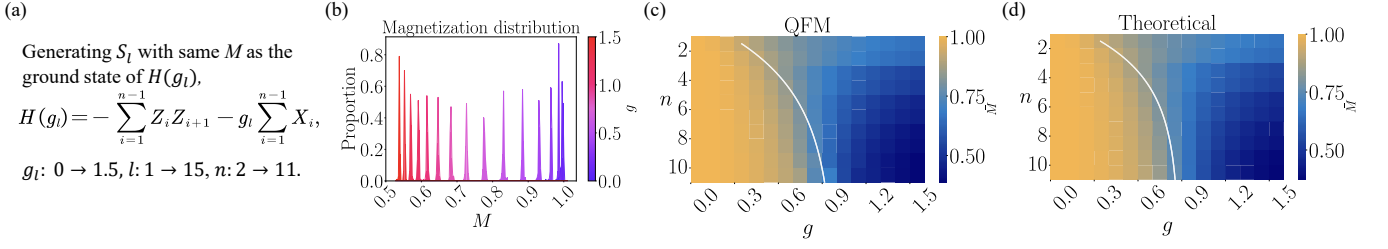


FIG. 11. Generation of magnetized state ensemble. (a) QFM is trained to generate state ensembles of different magnetization M under various magnetic field strengths g . (b) Magnetization distribution of the ensemble generated at each step in a 4-qubit system, denoted by color. (c) The transition line (white) and the average magnetization \bar{M} for various system sizes n and g , which closely matches the theoretical result in (d).

We apply QFM to generate the ground state ensemble $S_\tau = \{|\tilde{\psi}_\tau^m\rangle \mid |\tilde{\psi}_\tau^m\rangle = U(\vec{\theta}_\tau^{op})|\tilde{\psi}_{\tau-1}^m\rangle\}$ of $H(1.5\tau/L)$, where $\tau = 1 \rightarrow 15$. The loss function of step l is $D(\vec{\theta}_\tau^{op}) = (1/M) \sum_{m=1}^M \langle \tilde{\psi}_{\tau-1}^m | V^\dagger(\vec{\theta}_\tau) | H(1.5\tau/\mathcal{T}) | V(\vec{\theta}_\tau) | \tilde{\psi}_{\tau-1}^m \rangle$. As shown in Fig. 11b, we demonstrate the performance in a 4-qubit system, generating ground state ensembles with QFM and measuring magnetization $M = (\sum_i \sigma_z^i)/n$. In contrast to QuDDPM, which only generates the state ensemble with specific magnetization, QFM can track the varying magnetization \bar{M} of the state ensemble, as shown in Fig. 11c with various qubits $n = 2 \rightarrow 11$ and field strengths $g = 0.0 \rightarrow 1.5$, which matches the theoretical result (Fig. 11d).